



# DESIGN AND OPTIMIZATION OF LATTICE STRUCTURES FOR AEROSPACE APPLICATIONS

Enrico Stragiotti

François-Xavier Irisarri<sup>1</sup>, Cédric Julien<sup>1</sup> and Joseph Morlier<sup>2</sup>

1: ONERA - The French Aerospace Lab  
DMAS - Département matériaux et structures  
92320 Châtillon, France  
[{francois-xavier.irisarri, cedric.julien}@onera.fr](mailto:{francois-xavier.irisarri, cedric.julien}@onera.fr)

2: ICA - Institut Clément Ader  
ISAE - SUPAERO  
31400 Toulouse, France  
[joseph.morlier@isae-supraero.fr](mailto:joseph.morlier@isae-supraero.fr)  
January 29, 2024

PhD manuscript

ONERA – ISAE Supaero

## **Colophon**

This document was typeset with the help of KOMA-Script and L<sup>A</sup>T<sub>E</sub>X using the kaobook class.

ONERA – ISAE Supaero

# CONTENTS

<b>Contents</b>	<b>iii</b>
<b>List of Figures</b>	<b>v</b>
<b>List of Tables</b>	<b>v</b>
<b>List of Abbreviations</b>	<b>vi</b>
<b>1 Design of real-size aeronautical wing structures</b>	<b>1</b>
1.1 3D CRM wingbox with multiple load cases . . . . .	1
1.1.1 Advanced thresholding . . . . .	2
1.1.2 Numerical optimization of the CRM wingbox . . . . .	3
1.2 NACA 0012 modular drone wing . . . . .	12
1.2.1 Modular ground structure generation for irregular volumes . . . . .	12
1.2.2 Numerical optimization of the modular NACA 0012 drone wing . . . . .	13
1.3 Conclusion . . . . .	22
<b>Bibliography</b>	<b>23</b>



## LIST OF FIGURES

1.1	(a) Ground structure of the CRM-315 test case; (b) Ground structure of the CRM-2370 test case. The cross-sectional areas shown in the two sub-figures represent the starting point of the optimizations. . . . .	3
1.2	Optimized topology of the CRM-315 with 257 active bars. . . . .	4
1.3	Iteration history of the CRM-315 test case solved with the 2S-5R algorithm. (a) objective function history for the SLP and NLP step. The sharp increases in the objective function during the SLP step correspond to the reinitialization calls. (b) constraint violation for the NLP step. . . . .	5
1.4	Undeformed (gray) and deformed (black) shapes of the optimized CRM-315 structures with half wing span of 29.4 m for different values of maximum Z displacement $Z_{t,\ell}$ of the wing tip constraints. (a) $Z_{t,\ell} = 1$ m ; (b) $Z_{t,\ell} = 2$ m; (c) $Z_{t,\ell} = 3$ m; (d) no maximum displacement constraints. . . . .	6
1.5	. . . . .	8
1.6	. . . . .	8
1.7	Maximum stress constraint value (left) and buckling constraint value (right) plotted on the deformed shape of the optimized design (undeformed shape in light grey) of CRM-2370 for the three load cases: +2.5 g maneuver (a), -1 g maneuver (b), and cruise with gust (+1.3 g) (c). The maximum z tip deflection is 4.167 m, -2.953 m, and 1.948 m, respectively. . . . .	10
1.8	Iteration history of the CRM-2370 example solved with the 2S-5R algorithm. (a) objective function history for the SLP and NLP step. The sharp increases in the objective function during the SLP step correspond to the reinitialization calls. (b) constraint violation for the NLP step. . . . .	11
1.9	Normalized buckling and maximum stress constraint values for the optimized CRM-2370 structure after the SLP and the NLP optimization steps. . . . .	11
1.10	[14] . . . . .	12
1.11	. . . . .	14
1.12	. . . . .	15
1.13	. . . . .	15
1.14	. . . . .	18
1.15	. . . . .	18
1.16	. . . . .	19
1.17	. . . . .	20
1.18	. . . . .	21

## LIST OF TABLES

1.1	Material data used for the CRM optimization. . . . .	2
1.2	Numerical results of the optimization of the CRM with two different ground structures.	5

1.3	remember put here the span of the wing . . . . .	6
1.4	remember put here the span of the wing . . . . .	7
1.5	remember put here the span of the wing . . . . .	7
1.6	Number of active mechanical failure constraints for the CRM-2370 optimized design per type of constraint (rows) and per load case (columns). . . . .	9
1.7	Material data of the Ultem 2200 used for the NACA 0012 optimization. . . . .	12
1.8	Numeric results of the parametric study on the influence of the number of modules $N_T$ on the NACA 0012 drone wing. . . . .	15

## LIST OF ABBREVIATIONS

<b>CFRP</b>	Carbon Fiber Reinforced Polymer
<b>CRM</b>	NASA Common Research Model
<b>FEA</b>	Finite Element Analysis
<b>LP</b>	Linear Programming
<b>MILO</b>	Mixed-Integer Linear Optimization
<b>NLP</b>	Non-Linear Programming
<b>SLP</b>	Sequential Linear Programming

Ultralight trusses are a good design candidate for the design of innovative aerostructures thanks to their superior aeroelastic properties and stiffness-to-weight ratio. These structures represent a natural application case for the discussed optimization formulations until that point [1]. Opgenoord [2, 3] proposed a two-step sequential optimization algorithm to reduce the weight of a truss wing. Firstly, a ground structure with different nodal densities based on the stress field of the structure is generated and secondly, the cross-sectional areas are found using a sizing optimization algorithm that takes into account stress, local buckling, and aeroelastic constraints. Shahabsafa [4] decided, instead, to tackle all the difficulties of the problem using a set of discrete cross-sectional areas and a sizing Mixed-Integer Linear Optimization (MILP) algorithm. In these studies, the adoption of a sizing optimization algorithm simplifies the numerical complexities associated with the problem. However, by solely focusing on modifying the component sizes, the opportunity to optimize the overall truss topology is missed, limiting the potential for further weight savings. Additionally, no one of these studies evaluated the feasibility of the proposed design. It is here that the modularity could be beneficial.

In the preceding chapters we focused on the development of optimization methods for monolithic and modular structures, and we applied them to two and three dimensional academic load cases. Here we want to validate the proposed optimization algorithms by testing them on real world engineering problems in the aeronautic domain. First, to assess the computational efficiency and to validate the strategy proposed in Chapter ?? on a large-scale structure, we optimize a monolithic three-dimensional wingbox test case based on the NASA Common Research Model (CRM) with multiple load cases and for two discretization refinements. Later, we put the modular algorithm presented in Chapter ?? on a drone-sized wing based on a extruded NACA 0012 profile.

The optimizations presented in this section are performed on a notebook equipped with an Intel Core™ i5-9400H Processor @ 2.50 GHz (4 cores) and 16 GB of RAM.

## 1.1 3D CRM WINGBOX WITH MULTIPLE LOAD CASES

In this section, the proposed strategy is used to optimize a real-size wingbox, to validate its ability to work on large, three-dimensional structures with more candidate members compared to the precedent

1.1 3D CRM WINGBOX WITH MULTIPLE LOAD CASES . . . . .	1
1.2 NACA 0012 MODULAR DRONE WING . . . . .	12
1.3 CONCLUSION . . . . .	22

1. Cramer et al. (2019), 'Elastic shape morphing of ultralight structures by programmable assembly'
2. Opgenoord et al. (2018), 'Aeroelastic Tailoring using Additively Manufactured Lattice Structures'
3. Opgenoord et al. (2019), 'Design for additive manufacturing: cellular structures in early-stage aerospace design'
4. Shahabsafa et al. (2018), 'A novel approach to discrete truss design problems using mixed integer neighborhood search'

5. Brooks et al. (2018), 'Benchmark Aerostructural Models for the Study of Transonic Aircraft Wings'
6. Fakhimi et al. (2021), 'Discrete multi-load truss sizing optimization'
7. Stragiotti (2023), 'Truss Topology Optimization with Topological Buckling Constraints Data Set'

Parameter	Value
$E$	69 GPa
$\sigma_c, \sigma_t$	$\pm 270$ MPa
$\rho$	$2.7 \text{ g cm}^{-3}$

**Table 1.1:** Material data used for the CRM optimization.

8. Diamond et al. (2016), 'CVXPY: A Python-Embedded Modeling Language for Convex Optimization'
9. Domahidi et al. (2013), 'ECOS: An SOCP solver for embedded systems'
10. Moore et al. (2018), 'cyipopt: Cython interface for the interior point optimizer IPOPT'
11. Wächter et al. (2006), 'On the implementation of an interior-point filter line-search algorithm for large-scale nonlinear programming'
12. Alappat et al. (2020), 'A Recursive Algebraic Coloring Technique for Hardware-efficient Symmetric Sparse Matrix-vector Multiplication'

Equation ?? reads:

$$\phi_n = \phi_{n-1}^\beta \quad \forall n \in [1, \dots, n_{\max}],$$

with  $\phi_0 = 0.8$  and  $\beta = 2$ .

test cases. The structure is based on the jig (undeformed) shape of the wingbox of the NASA NASA Common Research Model (CRM) [5]. The structure is submitted to three different load cases: +2.5 g maneuver (LC\_1), -1 g maneuver (LC\_2), and cruise with gust +1.3 g (LC\_3). The nodes of the bounding volume and the loads used are provided by Fakhimi *et al.* [6], where a detailed discussion on how they are evaluated can be found. The ground structure of the test case is presented in Fig. 1.1a. Additionally, the load cases and the starting point, of all the presented test cases are available in the reference data set [7].

The material used for the optimization is an aluminum alloy with Young's modulus of 69 GPa, density of  $2.7 \text{ g/cm}^3$ , and yield stress equal to  $\pm 270$  MPa (see Table 1.1). To ensure a conservative design, we incorporated safety factors ( $sf$ ) associated with each load case. These safety factors are integrated into the formulation by reducing the maximum stress and buckling allowables by factors of 1.5, 1.5, and 2.67 for the three considered load cases, respectively. The cross-sections are assumed circular with the cross-sectional buckling parameter  $s = \pi E / 4$ . The optimization is carried only on the wingbox, the internal structure of the wing, and there is no influence of the skin on the optimization.

The optimizations are performed using the Python package CVXPY 1.2.2 [8] with the ECOS 2.0.7 [9] solver to solve the relaxed Linear Programming (LP) Problem Equation ???. The Non-Linear Programming (NLP) Problem Equation ??? is solved using cyipopt [10], a Python wrapper for IPOPT 3.14.11 [11], a large-scale nonlinear optimization package using PARDISO 6.0 [12] as the linear solver. The Jacobian and the Hessian of the Lagrangian of the NLP step are calculated at every optimization iteration to allow faster convergence. As every state variable of the optimization is independent of the others, these responses are derived analytically and will not be detailed there. The stopping criterion used for the Sequential Linear Programming (SLP) and NLP optimisations are  $\|\Delta x\|_\infty \leq \text{tol}_{slp}$ , and  $\|\Delta_{NLP}\|_\infty \leq \text{tol}_{nlp}$ , with  $\text{tol}_{slp} = 10^{-6}$  and  $\text{tol}_{nlp} = 10^{-4}$  respectively.  $\Delta_{NLP}$  represents the scaled NLP error, a more comprehensive value used by IPOPT to take into account the optimality of the solution and the constraints violation. The reinitialization magnitude parameter  $\phi$  is set up using Equation ??, leading to  $\phi = [0.8000, 0.6400, 0.4096, 0.1677, 0.0281]$  for the five reinitialization calls of 2S-5R. The full list of parameters used to set up the variable scaling, the SLP optimization, the reinitialization, and the NLP optimization is the same used in Chapter ?? listed in Table ??.

### 1.1.1 ADVANCED THRESHOLDING

As the CRM is a large and thin structure that presents a noticeable difference in load magnitude between the tip and the root of the

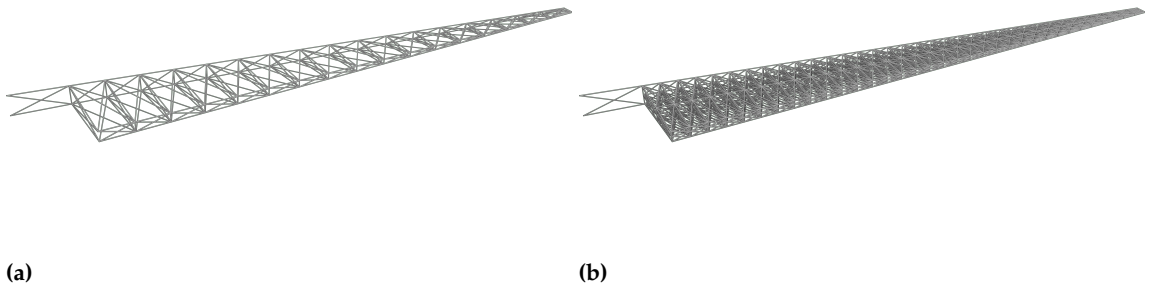


**Figure 1.1:** (a) Ground structure of the CRM-315 test case; (b) Ground structure of the CRM-2370 test case. The cross-sectional areas shown in the two sub-figures represent the starting point of the optimizations.

wingbox, the quantities of interest of the optimization span different orders of magnitude (from  $\text{m}^2$  to  $\text{mm}^2$ , and from  $\text{MN}$  to  $\text{N}$ ). For that reason, the choice of the cross-sectional area threshold value  $\chi$  defined in Equation ?? and used to simplify the initial NLP ground structure is crucial. Taking a high value (such as  $\chi = 10^{-4}$ , restraining the solution from  $\text{m}^2$  to  $\text{cm}^2$ ) would mean possibly canceling out bars fundamental for the nodal force equilibrium in the less loaded part of the wing (wing tip and the central part of the wing's sections near the root). By contrast, a low value (such as  $\chi = 10^{-9}$ ) would permit the correct simulation of the mechanical response of the structure, but it would lead to a very high number of candidate bars and, thus, longer optimizations and convergence difficulty for the NLP phase. For that reason,  $\chi$  is set to an average value ( $\chi = 10^{-6}$ ), eliminating all the bars under the value  $a_{\text{thr}} = \chi \max(\mathbf{a})$ , but an additional check is performed before proceeding to the thresholding. The bars under the threshold  $a_{\text{thr}}$  are sorted in ascending order of cross-sectional area and, starting from the smallest one, we iteratively check via a Finite Element Analysis (FEA) that the difference between the force and displacement fields before and after the bar removal is below than a certain bound. In the present study we used the following:  $\|\Delta q\|_\infty < 10 \text{ N}$  and  $\|\Delta U\|_\infty < 1 \text{ cm}$ .

Equation ?? reads:

$$a_i < a_{\text{thr}} \quad \forall i, \text{ with } a_{\text{thr}} = \chi \max(\tilde{\mathbf{a}}^*)$$

### 1.1.2 NUMERICAL OPTIMIZATION OF THE CRM WINGBOX

Two different discretizations are considered for the optimization. The proposed algorithm is firstly tested on the same ground structure provided by Fakhimi *et al.* [6], composed of  $N_{\text{el}} = 315$  candidate members (CRM-315). The second discretization is obtained by refining the 315-bar ground structure, evaluating the midpoints of every member, and connecting them with first-order connectivity. We obtain  $N_{\text{el}} = 2370$  candidate members (CRM-2370). The loads and the boundary conditions are applied on the same nodes of the ground structure for the two studied ground structures. The cross-sectional areas of the starting point of the CRM-315 and the CRM-2370 are set

6. Fakhimi et al. (2021), 'Discrete multi-load truss sizing optimization'

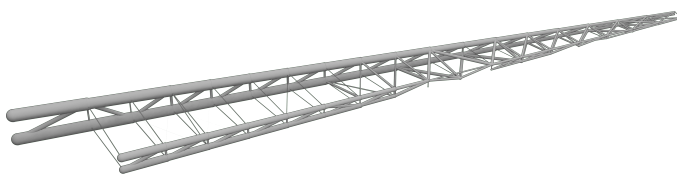


**Figure 1.2:** Optimized topology of the CRM-315 with 257 active bars.

to  $0.0001 \text{ m}^2$  and they are shown in Fig. 1.1. Only one single start point is used for these two examples as the proposed two-step strategy with reinitialization already proved in Chapter ?? to reduce the starting point influence on the optimization result. The resolution algorithm used is 2S-5R. The numerical results of the optimization for the two different discretizations are reported in Table 1.2.

The optimized CRM-315 structure shows a mass of 21.342 t, a 27.01 % reduction compared to the solution with discrete cross-section areas found by Fakhimi *et al.* [6] (29.238 t). Other than the substantial difference in the modelization of the cross-section areas, the mass reduction could be explained by the fact that the proposed algorithm has a zero lower bound on cross-sectional areas, thus permitting the topology of the structure to change: the 2S-5R solution shows 257 active bars out of 315 at convergence (see Fig. 1.2). In contrast, the MILO problem solved by Fakhimi *et al.* [6] is employed as a sizing optimization algorithm with fixed topology (and thus 315 active members in the optimized design). A more detailed comparison could not be performed as the authors did not share the values of the cross-sectional areas of their solution.

The volume fraction of the solution is 1.313 % and the minimum slenderness ratio  $\lambda$  (ratio between the length and the radius of gyration of the bar) of a bar is 14.96, which is compatible with the truss modelization used to discretize the wingbox volume. The execution time of the optimization is 19 s for the SLP step and 128 s for the NLP step, for a total of 147 s on a regular notebook, compared to the over four days of optimization of Fakhimi [6] on a desktop workstation. The iteration history curves of the optimization are plot in Fig. 1.3a, in which we notice the sharp volume increase due to the reinitialization heuristic in the SLP step. Fig. 1.3b shows invece the constraint violation curves for the NLP phase. The starting point coming from the relaxed SLP step violates the stress and buckling constraints as the predicted force field does not account for kinematic compatibility, necessary due to the multiple loading condition of this test case. From the graph we can notice how the kinematic compatibility constraint is extremely hard to satisfy.

6. Fakhimi et al. (2021), 'Discrete multi-load truss sizing optimization'

Quantity	CRM-315	CRM-2370
$N_{el}$	315	2370
$N_{opt}$	257	1127
$V [m^3]$	7.90	7.44
$V [\%]$	1.309 %	1.232 %
Mass [t]	21.342	20.092
$a_{max} [m^2]$	0.198	0.208
$C_{LC\_1} [MJ]$	3.23	3.17
$C_{LC\_2} [MJ]$	1.28	1.27
$C_{LC\_3} [MJ]$	0.76	0.74
$t [s]$	147	3189

**Table 1.2:** Numerical results of the optimization of the CRM with two different ground structures.

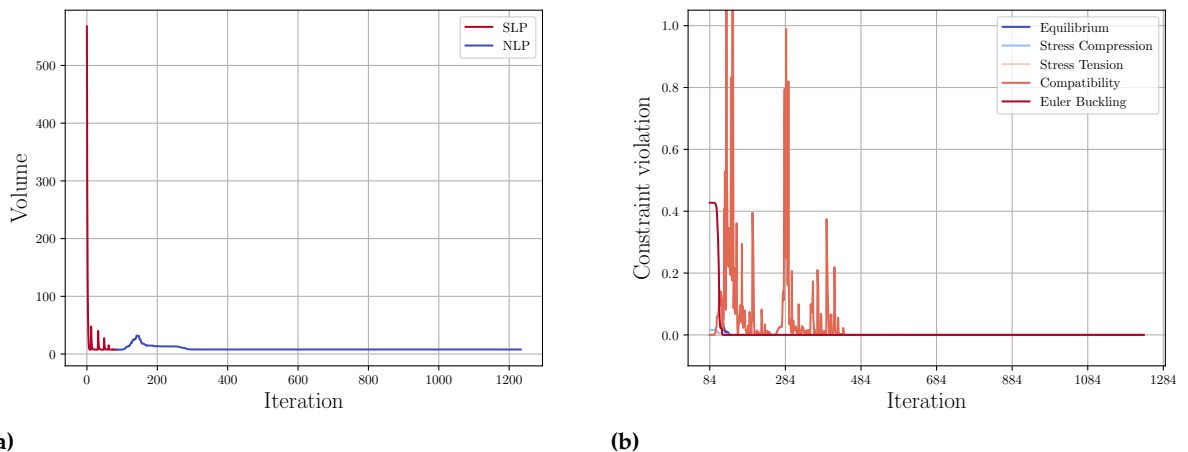


**Figure 1.3:** Iteration history of the CRM-315 test case solved with the 2S-5R algorithm. (a) objective function history for the SLP and NLP step. The sharp increases in the objective function during the SLP step correspond to the reinitialization calls. (b) constraint violation for the NLP step.

**MAXIMUM DISPLACEMENTS CONSTRAINTS** The designer of a plane could be interested in limiting the maximum Z displacement  $Z_{t,\ell}$  of the wing tip to avoid a too high flex on the wing that could influence too much the aerodynamic field attorno all ala. We remember that controlling the displacements of the structure, we can actively influence the compliance of the structure, even if the compliance minimization is not in the objective function. Additionally, this could be a constraint that can passively add stiffness to the wing and helps with the aeroelastic phenomenon of flutter instability.

having observed that in the unconstrained version the maximum tip displacement of the optimized CRM-315 structure, that has a half wing span of 29.4 m, is  $Z_t = 4.11$  m, we set three different  $Z_{t,\ell} = [1 \text{ m}, 2 \text{ m}, 3 \text{ m}]$  in the NLP step, willing to explore how sensible is the optimized structure is with respect to this constraint. The optimization are efectuated using the same material, geometrical and load data used in the above example.

We plot the displacements in the XZ plane in Fig. 1.4 and the numeric

**Table 1.3:** remember put here the span of the wing

$Z_{t,\ell}$ [m]	1	2	3	-
$V$ [ $\text{m}^3$ ]	26.70	13.78	9.39	7.90
$V$ [%]	4.421 %	2.283 %	1.556 %	1.309 %
Mass [t]	72.086	37.218	25.363	21.342
$a_{\max}$ [ $\text{m}^2$ ]	0.615	0.293	0.197	0.198
$C_{LC\_1}$ [MJ]	1.05	1.96	2.79	3.23
$C_{LC\_2}$ [MJ]	0.37	0.71	1.04	1.28
$C_{LC\_3}$ [MJ]	0.26	0.47	0.67	0.76

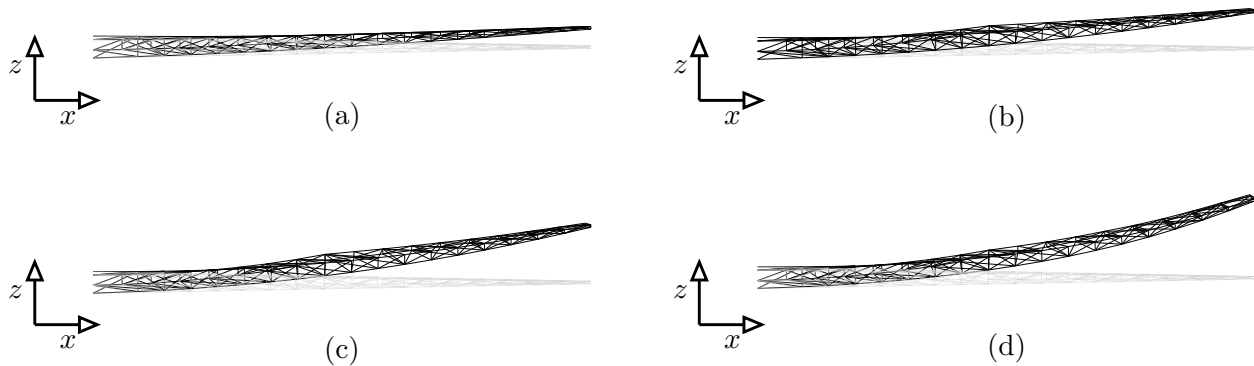


**Figure 1.4:** Undeformed (gray) and deformed (black) shapes of the optimized CRM-315 structures with half wing span of 29.4 m for different values of maximum  $Z$  displacement  $Z_{t,\ell}$  of the wing tip constraints. (a)  $Z_{t,\ell} = 1$  m ; (b)  $Z_{t,\ell} = 2$  m; (c)  $Z_{t,\ell} = 3$  m; (d) no maximum displacement constraints.

We remember that the CRM shows a half wing span of 29.4 m.

values of the optimization in Table 1.3. First, we notice how efficacely the optimizer limited the maximum displacement and converged to a solution even with a hard to satisfy constraint as  $Z_{t,\ell} = 1$  m . Second, we see that the constraint satisfaction doesent come free. The added rigidity needed to comply with the maximum displacement constraint come from a massive add of material that represent a 19 percent, 75 percent and 237 percent increase for the  $Z_{t,\ell} = [3 \text{ m}, 2 \text{ m}, 1 \text{ m}]$ , respectively. Finally, as already stated before, the constraints on the maximum displacements infuence a lot the compliance of the structure, and we can see how, even if the proposed formulation does not keep into account for that, we can reduce indreclly the compliance of the structure.

**MULTIPLE MATERIALS** The proposed formulation uses the material data as an input for the optimization and up untill this point we never interested in seeing how the mateial data could influence the topology and the final volume of the optimized structure. However we know how much the material is important and we wnat here see the influence on the CRM-315 test case.

We used four different materials commonly used in the aerospace domain: an alluminium alloy, titanium alloy, inox steel and pultruted Carbon Fiber Reinforced Polymer (CFRP), of which mecanical properties are reported in Table 1.4. on the top of classic material properties as young modulus, yeld stress and density we also take into account the

Material	Aluminium	Titanium	Steel	Pultruted CFRP
$E$	69 GPa	120 GPa	210 GPa	150 GPa
$\sigma_c, \sigma_t$	$\pm 270 \text{ MPa}$	$\pm 880 \text{ MPa}$	$\pm 355 \text{ MPa}$	$+1200, -880 \text{ MPa}$
$\rho$	$2.7 \text{ g cm}^{-3}$	$4.5 \text{ g cm}^{-3}$	$7.8 \text{ g cm}^{-3}$	$1.6 \text{ g cm}^{-3}$
$\text{kgCO}_e^2/\text{kg}$	12.5	47.0	5.0	34.5
\$/\text{kg}	2.2	23.5	6.3	40.5

**Table 1.4:** remember put here the span of the wing

Material	Aluminium	Titanium	Steel	Pultruted CFRP
$V [\text{m}^3]$	7.90	4.53	5.88	3.67
$V [\%]$	1.309 %	0.749 %	0.974 %	0.607 %
Mass [t]	21.342	20.372	46.168	5.868
$a_{\max} [\text{m}^2]$	0.198	0.088	0.153	0.086
$C_{LC\_1} [\text{MJ}]$	3.23	4.88	1.33	4.39
$C_{LC\_2} [\text{MJ}]$	1.28	1.94	0.53	1.73
$C_{LC\_3} [\text{MJ}]$	0.76	1.15	0.31	1.03
$Z_t [\text{m}]$	4.10	5.97	1.70	5.31
Cost [ $\text{tCO}_e^2$ ]	266.7	957.5	230.8	202.4
Cost [k\$]	46.9	478.7	290.8	237.6

**Table 1.5:** remember put here the span of the wing

enviromental cost i.e. the mass of equivalent co2 emitted to produce a unit mass of the material and also the economic cost in dollar. We took this value from the book of Ashby [13].

The numerical results are presented in Table 1.5 and different observation can be made. First, we confirm that the mass of the optimized structure is highly influenced by the material choice, and more exactly it seems particularlly influenced by the specific resistance and specific stiffness of the material. Second we notice that also the value of the compliance and the maximum tip displacement is very influenced by material data, and more exactly elle est pilotée par le rapport entre strenght and young modulus of the material. This because with a material more strong we have smaller cross sectionals areas and thus smaller global rigidity. Third, is the volume behaviour, that follows a hyperbolic law with respect to the strenght of the material (as in this specific case the most volumic elements are constraint by stress and not buckling, see the constraints analysis later in the chapter). We finally give the deformed structures in Fig. 1.5, in wich we clearly see how the titanium and the pultruted cfrp shows high deform shapes due to their high material properties.

[13. Ashby (1999), 'Materials selection in mechanical design'

We then observe the environmental and economic cost of the 4 structures. having a look at Fig. 1.6, we notice how, a part from titanium, the structures shows almost the same environmental cost for the production of the material. this come as unexpected due to the very different spectific c02 emission e.g. there is a difference of almost 7 times between steel and CFRP. However the cfrp solution shows a massively reduction in weight that at the end favours it with respect to steel and even aluminum. A similar result can be observed in cost, anche se the very low production cost favors aluminum with respect

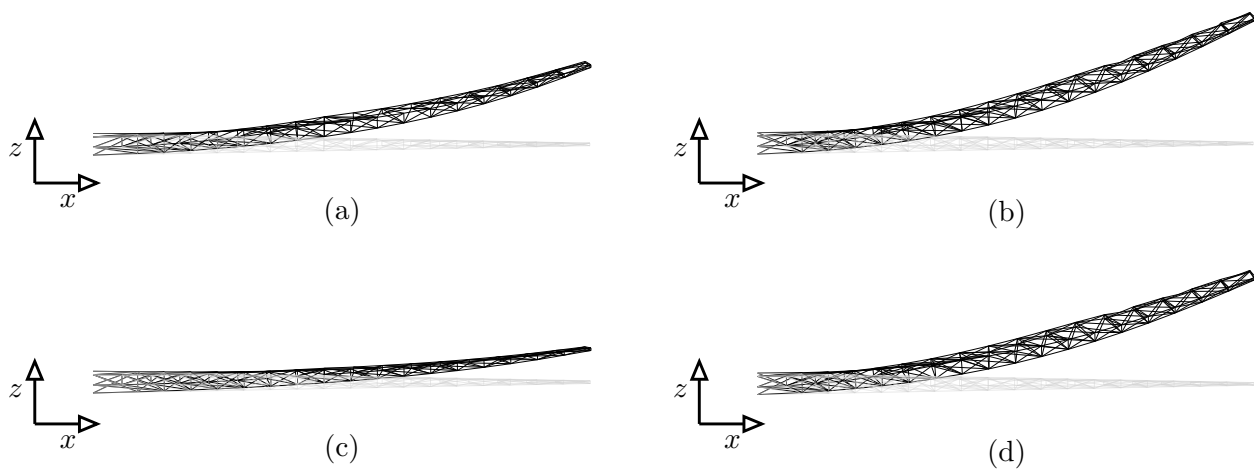


Figure 1.5

to all other materials. It seems that at the end for this specific load case, the CFRP, even if costing more than aluminium, represent the better compromise between excellent mechanical properties, environmental and economic cost. Finally, ovviamente qui si tiene in conto solo del costo del materiale, ma il peso inferiore su un aero permette di risparmiare veramente molto di piu rispetto al costo della sola produzione. questo favorisce ancora di piu il caso pultruded CFRP.

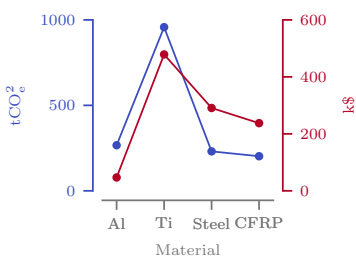


Figure 1.6

**ENRICHING THE MESH** As earlier described in the chapter, we want now to assess the influence of the initial ground structure on the volume and topology of the optimized structure. We use then the refined ground structure called CRM-2370, optimized for the smae threhee load cases used precedently and using the aluminium as material.

The mass of the optimized CRM-2370 structure is 20.092 t, a 1.318 t reduction compared to the CRM-315 (−6.2%). Additionally, if we compare the compliance of the three load cases (see Table 1.2), we notice how the solution of CRM-2370 is not only lighter but also stiffer, suggesting in general a more efficient structure topology. The maximum [sostituisceci con Zell] z tip deflection of the wingbox is 4.167 m, −2.953 m, 1.948 m for the three considered load cases, respectively. There are 1127 active bars in the optimized design, and the whole optimization took 3189 s (1911 s for the SLP step, 1278 s for the NLP step). The iteration history curves of the optimization are plot in Fig. 1.8. In Fig. 1.7 the normalized maximum stress and buckling constraints are plotted on the deformed shape of the three load cases. We notice how in general the topology of the two external "spars" is shaped after the +2.5 g load case, while the interior of the wingbox is made by a thinner truss constrained by buckling.

	<b>LC_1</b>	<b>LC_2</b>	<b>LC_3</b>	<b>Tot.</b>
<b>Buckling</b>	281	145	143	569
<b>Tension</b>	56	3	4	63
<b>Compression</b>	286	6	6	298
<b>Tot.</b>	623	154	153	930

**Table 1.6:** Number of active mechanical failure constraints for the CRM-2370 optimized design per type of constraint (rows) and per load case (columns).

**ACTIVE MECHANICAL CONSTRAINTS** To better understand which mechanical phenomena is the most constraining for the bars of the solution, we present in Fig. 1.9 a graph where the normalized stress criterion  $c_s = \max(-q sf/\sigma_c a, q sf/\sigma_t a)$  and the normalized buckling criterion  $c_b = q sf/q_{\text{crit}}$  are plotted against each other. Every point in the scatter plot represents the members of the solution of the SLP and the NLP steps that show at least a charge of 1N (931 out of 1127 members). This threshold is applied as at the end of the NLP step some members present a very small section, creating numerical problems when evaluating the stress and buckling criteria. All the SLP members activate either the maximum stress or buckling limit, while 68 out of 931 NLP members are located in the center of the graph ( $c_s < 0.95$  and  $c_b < 0.95$ ). We speculate that this behavior is due to the inclusion of the kinematic compatibility constraint in the NLP algorithm: the cross-sectional area of these bars is chosen to comply with the global displacements. In Table 1.6, a summary of the active mechanical failure constraints (buckling, tensile stress, and compressive stress) present in the NLP solution. The table showcases the number of active constraints categorized by constraint type and load case. The optimized design encompasses a total of 930 active mechanical failure constraints for 863 bars (931 minus the 68 bars constrained by kinematic compatibility). This suggests that certain members are concurrently subject to multiple failure constraints across different load cases. An additional observation is that the design of the solution is primarily influenced by local buckling and compressive failures, especially under the +2.5 g load case (LC\_1).

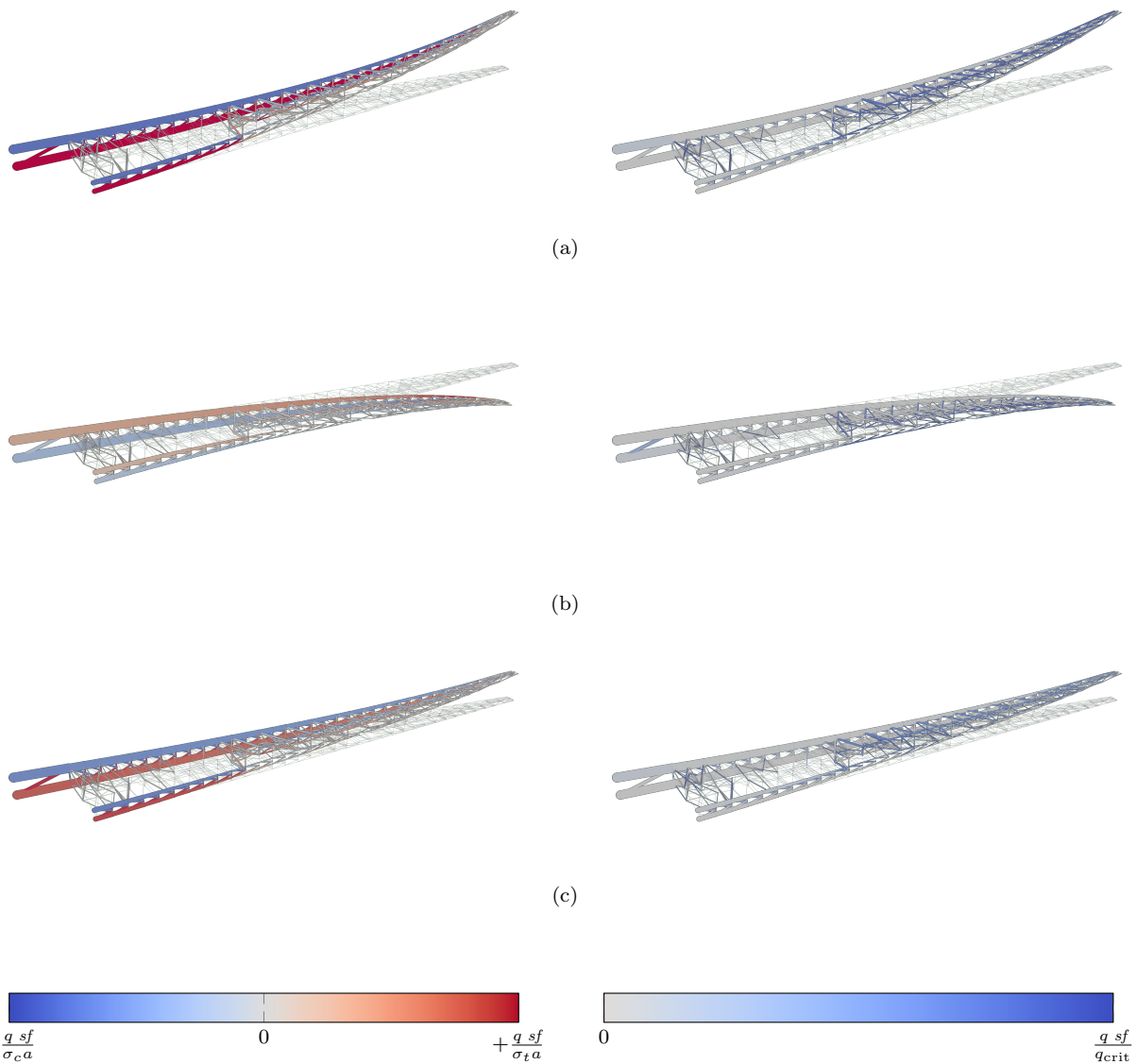


**Figure 1.7:** Maximum stress constraint value (left) and buckling constraint value (right) plotted on the deformed shape of the optimized design (undeformed shape in light grey) of CRM-2370 for the three load cases: +2.5 g maneuver (a), -1 g maneuver (b), and cruise with gust (+1.3 g) (c). The maximum  $z$  tip deflection is 4.167 m, -2.953 m, and 1.948 m, respectively.

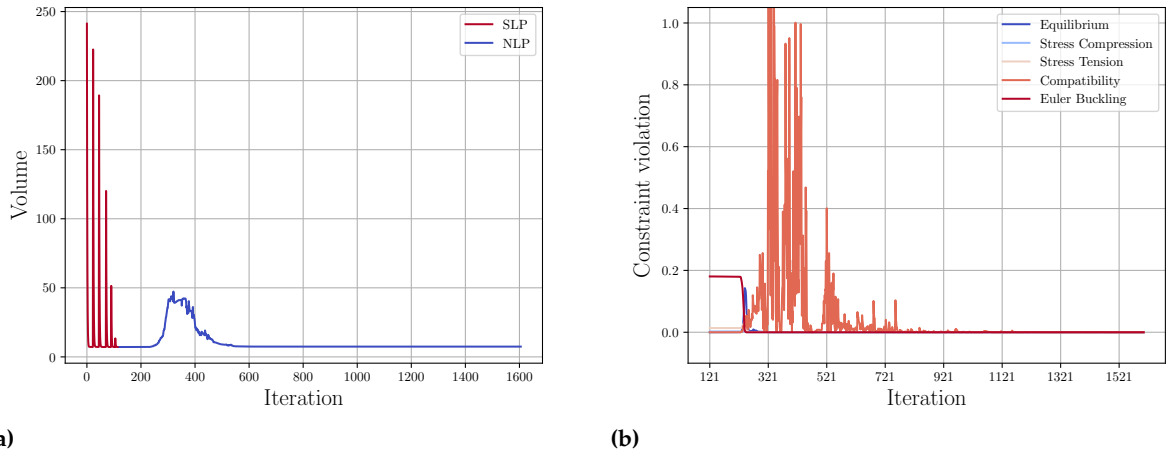


**Figure 1.8:** Iteration history of the CRM-2370 example solved with the 2S-5R algorithm. (a) objective function history for the SLP and NLP step. The sharp increases in the objective function during the SLP step correspond to the reinitialization calls. (b) constraint violation for the NLP step.

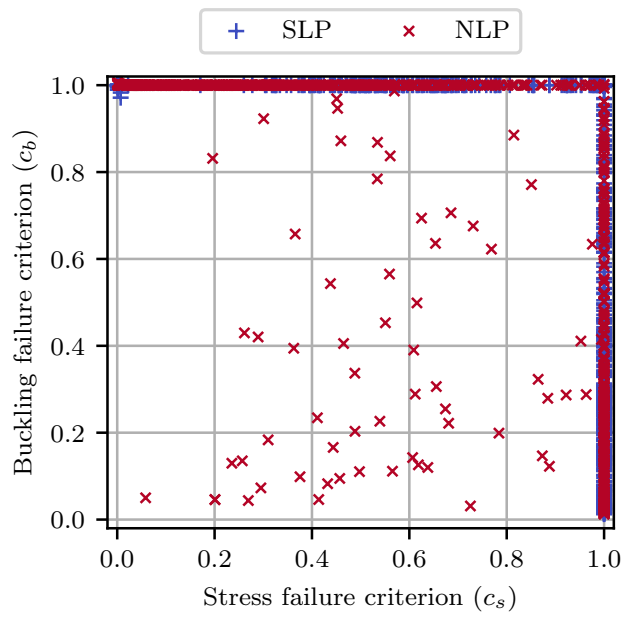


**Figure 1.9:** Normalized buckling and maximum stress constraint values for the optimized CRM-2370 structure after the SLP and the NLP optimization steps.

## 1.2 NACA 0012 MODULAR DRONE WING

Parameter	Value
$E$	6.8 GPa
$\sigma_c, \sigma_t$	$\pm 140$ MPa
$\rho$	$1.42 \text{ g cm}^{-3}$

**Table 1.7:** Material data of the Ultem 2200 used for the NACA 0012 optimization.

We will now deal with another aeronautical test case. One of the possible and most fitting application for modular structures is the use for small fixed wing drones. This is because of the easy in field deployment, easy to repair structure and extreme lightweight. Jenett and his working group at NASA developed an experimental platform for the study of active morphing wings using lattices which dimensions are shown in Fig. 1.10. The platform wing volume is obtained by extruding by  $b = 580 \text{ mm}$  a NACA 0012 airfoil with a chord  $c = 305 \text{ mm}$ . We are taking the exact same volume for our modular optimization, and instead of focussing on aerodynamic and aeroelastic properties, we deal with the optimization of the internal structure. As the platform was not meant for flying, the authors don't share additional data on the requirement used to design the internal structure. For that reason, we assume in a conservative way a MTOW = 10 kg and we design the structure to withstand a maximum loading factor  $n_z = 2$ . As the wing presents a rectangular planform on the XY plane we assume a constant lift distribution on the X axis (span of the extruded profile). As a further simplification, we assume the lift distribution as constant also on the Y plane (chord plane). The lift distribution is then integrated to evaluate the concentrated nodal load necessary to conduct our optimization. In this setting all the nodes on the upper skin are then equally loaded in the Z direction. As already done in the CRM test case, we don't take into account the effect of the skin on the mechanical model. The wing is encasted at the root points ( $X = 0$ ). Finally, the material used for the optimization is the Ultem 2200, a high-performance thermoplastic material filled at 20 % by glass fiber and known for its exceptional strength, heat resistance, chemical resistance, and suitability for applications requiring durability. The mechanical properties are summarized in Table 1.7.

### 1.2.1 MODULAR GROUND STRUCTURE GENERATION FOR IRREGULAR VOLUMES

Compared to the academic test cases presented in Chapter ?? and Chapter ??, the extruded NACA 0012 profile does not present a regular

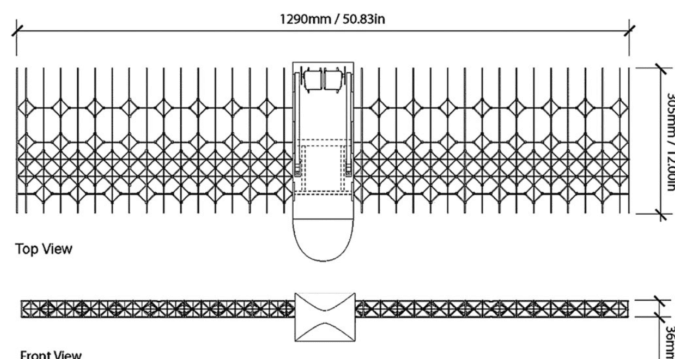


**Figure 1.10:** [14]

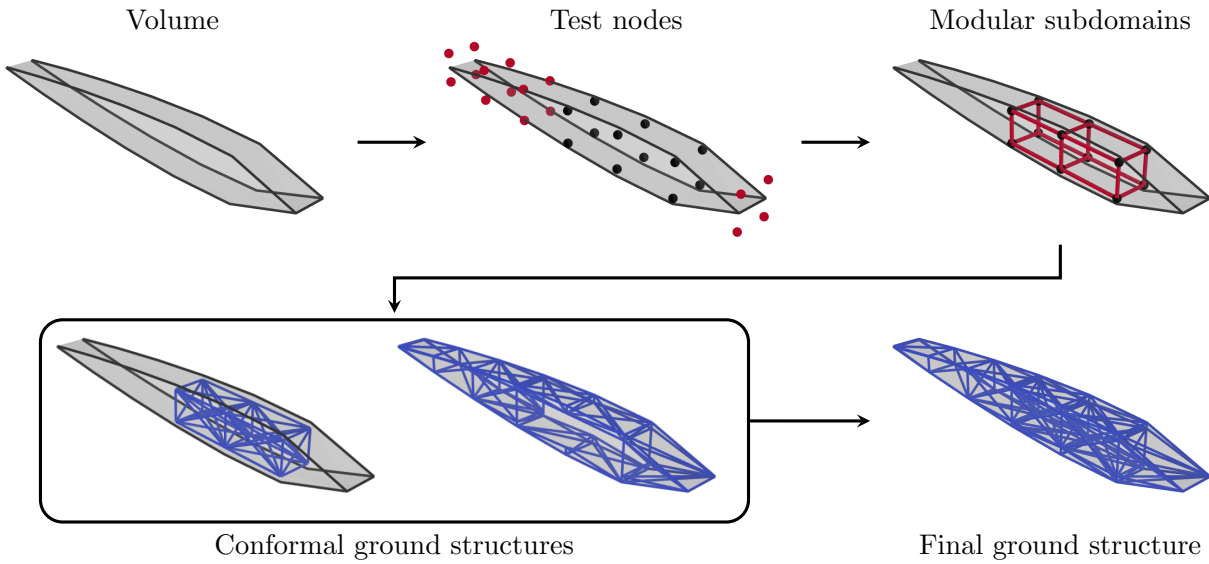
parallelepipedic shape that is easily partitioned in cubic subdomains. The easiest solution in this particular scenario of the extruded wingfoil case would be to partition the structure in sections by performing multiple cutting on the YZ plane, but this strategy would not apply to more complex external shapes. For that reason we developed a ground structure generation strategy that maximizes the generation of modular domains on complex volumes. First, we generate a cloud of nodes equally repartitioned in the three axis. The distance between nodes on the three axis represent an hyperparameter for the user that could via this parameter chose the size of the geometry of the repeating module. Then, the points are tested for their insideness inside the volume using a winding number algorithm. The winding number algorithm determines whether a point is inside or outside a polygon by counting the number of times a ray from the point crosses the polygon boundary. If the winding number is non-zero, the point is inside the polygon; otherwise, it is outside. The points that are inside the volume are grouped eight at a time and used as the vertex of the parallelepiped used as subdomains of the structure. Arrivati a questo punto, additional equispaced nodes are added inside the newly generated subdomains depending on the chosen module complexity. We have then now generated a modular subdivision of a complex volume, reducing at maximum the non-modular volume. All these phases are presented graphically on the upper line of Fig. 1.11.

Once in the structure we have identified the subdomains and generated the additional nodes, we can compute the modular ground structure. For each subdomain, a fully-connected ground structure is built. The ground structure of the remaining volume that was not filled with the subdomains is instead generated by employing the Delunay triangulation algorithm, using the edges of the generated tetrahedron as members of the ground structure. The role of this ground structure is essentially to transfer the loads from the external boundary to the modular structure, and it can be optimized concurrently with the modular structure. As the Delunay triangulation algorithm uses the nodes of the modular ground structure as seed for running the algorithm, the two discretizations are conformal. The final ground structure is simply given by superposing the two discretizations, taking care to eliminate the members of the non-modular part that sits on the faces of the modular part before. An example of the generation of the two conformal discretizations is given on the lower line of Fig. 1.11.

Remember, we defined the module complexity as the number of nodes used to generate the modules' ground structure.

### 1.2.2 NUMERICAL OPTIMIZATION OF THE MODULAR NACA 0012 DRONE WING

The just described algorithm is used to generate the ground structure used to optimize the modular NACA 0012 drone wing. In the specific case of the NACA 0012 wing the non-modular part is however very regular due to the extruded nature of the wing volume. For that

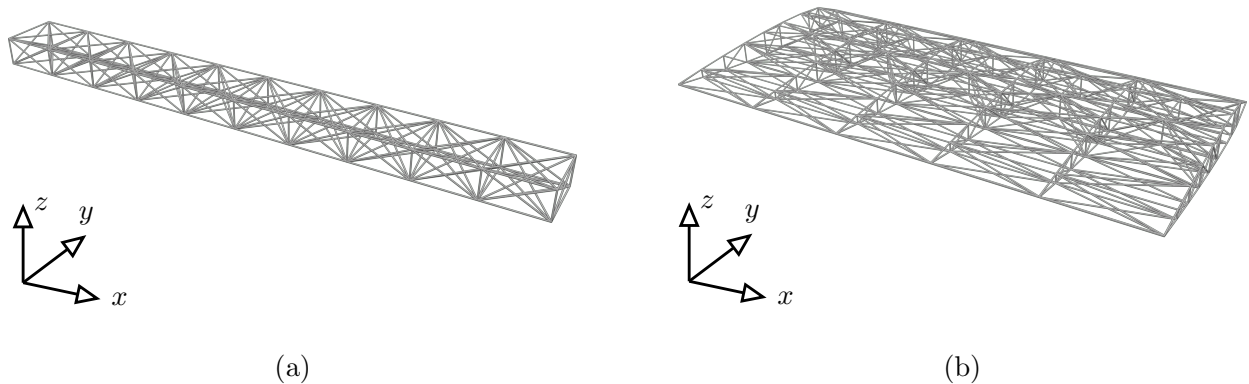
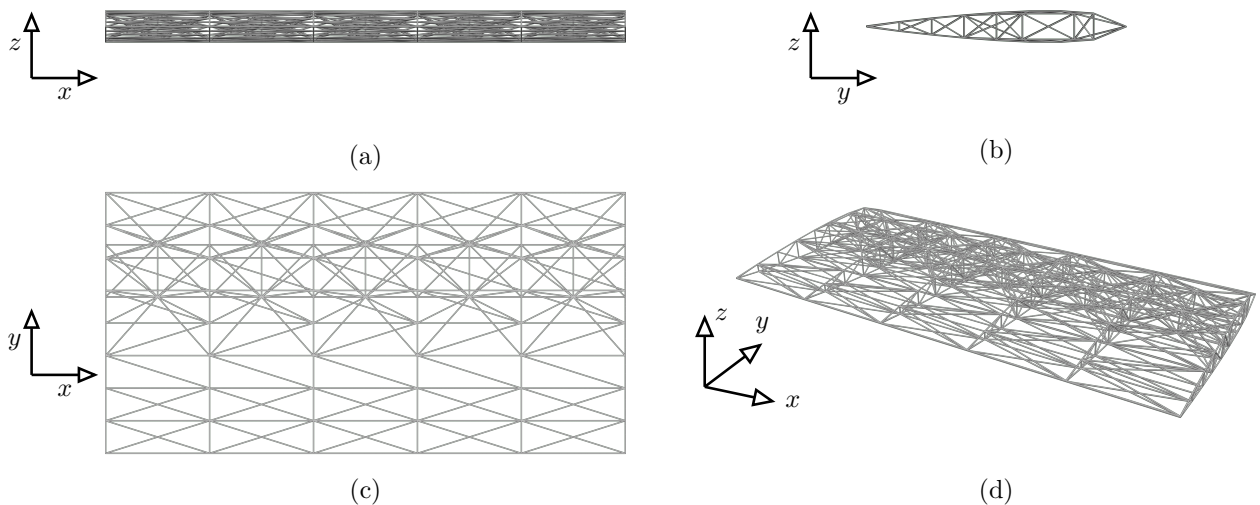
**Figure 1.11**

reason, the Delaney triangularization algorithm can easily outputs a modular ground strcuture. in this example we define then two different module type: the internal structure of the wing profile,called wingbox type, as it acts as the wongbox of the wing nd is mabe by parallelepipedic-shaped subdomains, and the profile type, that subdivide the original volume in wing sections.

The cloud points interdistance used for the wingbox type ground structure generation is chosen is such a manner to obtain 10 subdomains on the X axis, 1 on Y and 1 on Z. Every subdomain is made by  $2 \times 2 \times 2$  nodes and a fully connected ground structure, totalling 28 candidate elements per module. Concerning the profile type module, the extruded volume is cut in 5,1,1 subdmains on the x,y, and z axis, respectively. Every module shows a total of 175 candidatres per module. A graphical representation of the two conformal ground structures is presented in Fig. 1.12, while a comprehensive view of the full ground structure is shown in Fig. 1.13. THis ground structure configuration is called configuration A.

The configuration A ground structure just presented is used as the discretization used to solve three different problems otimization. We setup all the problems using the Ultem 2200 material and the wing dimension, loading conditions, and the buondary condstitions described earlier in Section 1.2. the difference between the problems is the use of a differnte number of module topologies  $N_T$  for the trhee optimization. we will start by analyzing the optimized structure behaviouhr using a single topology  $N_T = 1$  for the two module's types, and then we increment to  $N_T = 2$  and  $N_T = 3$ .

Table 1.8 reports the numerical results of the optimization. Even if it is the objective function of the optimiaztion, in this table we do not

**Figure 1.12****Figure 1.13****Table 1.8:** Numeric results of the parametric study on the influence of the number of modules  $N_T$  on the NACA 0012 drone wing.

$N_T$	Configuration A			Configuration B		
	1	2	3	1	2	3
$N_{\text{opt}} (N_{\text{el}})$	425 (1155)	503 (1155)	366 (1155)	620 (1675)	539 (1675)	454 (1675)
Mass [g]	49.0	33.3	29.5	37.3	23.8	22.9
$V$ [%]	0.81	0.55	0.48	0.62	0.39	0.37
$\bar{\rho}$ [kg/m <sup>3</sup> ]	11.53	7.84	6.93	8.76	5.59	5.38
$\varphi$	22.5 %	37.9 %	56.0 %	19.0 %	36.9 %	50.0 %
$\psi$	0.45	0.69	0.73	0.46	0.70	0.72
t	39 s	5 m 6 s	2 m 3 s	2 m 28 s	3 m 32 s	5 m 1 s

report the volume value, but the mass and the mass density, as they are more understandable and have more physical meaning and useful and follows exactly the same trends of the volume, times a factor. Looking at the column relatives to the configuration A, we see that the trends observed in Chapter ?? are still valid: The mass density and the mass of the structure is monotonically descending with the number of different module topologies, reaching a minimum of  $M = 29.5 \text{ g}$  and  $\bar{\rho} = 6.93 \text{ kg/m}^3$ . This specific mass density  $\bar{\rho}$  value is typical of aerogels [13], and comparable to the values of the NASA's MADCAT experimental platform [1]. Similar trends are observable also on the performance parameters  $\varphi$  and  $\psi$ , that tend towards 100 % and 1.00, signaling a more efficient use of material in the solution. The number of active bars of the solution  $N_{\text{opt}}$  is environ 40 % of the members of the initial ground structure. Finally, the execution times never went over the five minutes mark.

We will comment now more in detail the topology of the less voluminous solution, the one obtained for  $N_T = 3$  that shows a mass  $M = 29.5 \text{ g}$ . Fig. 1.14 presents graphically the most interesting aspects of the modular structure. In subfigures (a) to (d), it is shown the 4 representative views of the structures seen from 4 different angles. We will comment the topology starting from the root (left part of the images) and gradually going towards the tip. Near the root of the wing we see how the algorithm places almost no members as all the nodes are encasted. Then, moving to the central part of the wing, we observe how the algorithm proposes a topology that is somewhat resembling to a classic wing configuration made by spars and ribs. A big spar runs the whole span of the wing at the upper half of the chord. In the first three sections is very voluminous due to the high compression loads of the upper skin of the wing. We see however how towards the tip of the wing, the single massive spar is splitted in two lighter spars, due to the reduction of the loads. Looking at the ribs, we notice how the thickness of these members are mostly equal no matter what the X value is. This is because their only job is to transfer the loads towards the more voluminous spars (so they do not take additional loads from the successive sections, as the spars do) and the loads on them is constant with the X axis. In the case of a wing with a different planform and thus a different lift distribution on the X axis, this should probably not be the case i.e. shorter ribs are less charged and then thinner. Interestingly, looking at subfigure (a) we see how the modules show a topology near the root is more constrained by buckling (and predilect then tension elements), while near the tip of the wing the topology is more and more symmetric.

Concerning the modules layout, we see in subfigures (e) and (f) how the algorithm suggests basically the similar but not equal layout strategy for the two modules type. For the wingbox type (subfigure (e)), we see an almost uniform distribution of the different module topologies ver

[13] Ashby (1999), 'Materials selection in mechanical design'

[1] Cramer et al. (2019), 'Elastic shape morphing of ultralight structures by programmable assembly'

the wing span, with only a single interesting subdomain, the forth one from the root, that show a differnt topology. This fact could be explained either by wanting to solve a connectivity problem with near subdomains, or either the optimizer stuck in a local minima. For the section type (subfigure (f)), the first subdomains, the one near the root, show a different topology with respect to the other. this is understandable as this is usually a subdomains that shows a very different load state respect to the central subdomains, it is a border effect caused by the boundary conditions. Tihs was someting we have already precedently experienced, see for example Fig. ??, in which the subdomains near the load showed a different topology. THe other remaining module topologies are more evenly distributed on the span on the wing.

Finally, in subfigures (g) and (h) we present the optimized structure divided into the wingbox type and the section type subdomains. It is especially interesting notice how in subfigure (g) the most voluminous component is the upper part of the long compressive spar made by first seven submodules. The same observation is made encore clearer looknig at the wingbox type optimized structure of the case with  $N_T = 1$  that is shown in Fig. 1.15. Knowing that the cross sectional area of this component is particularry sensible with the legnht of the members that compose it, ci chiediamo if modifing the ground structure could be beneficial for this specific load case For that reason we decided to test a different ground structure configuration in which, insetad of having 10 differnt submodules, we have 20, halving in that way the lenght of the most voluminous buckling constrained bars. The new wingbox ground structure is shown in Fig. 1.16. the section type ground structure generation parameters used are the same, and the ground structure is only different to accomodate the nodes generadet by the new wingbox ground structure. We call this ground strucutre configuration B.

the numeric results of the optimizations of configuration B are presented in the right hand side part of Table 1.8. How correctly predicted, the fact of having reduced the free effective buckling lenght of the membes that composed the main wing spar, helped reducing considerably the mass of the structure. We notice how the change of ground structure helps us achieve a 23 %, 28 %, and 22 % mass reduction compared to configuration A for the three number of topologies considered. the volume trends for the two configurations are plotted in Fig. 1.17. Despite the increase of candidates member, the optimization time interestingly staid the same, with no optimization again that went after the five minutues of caluclation time. It is important to remember that in Section ?? we observed that increasing the number of subdomains tends to increase the volume of the solution, but in this specific test cse, we observe a different bahaviour. this fact confirs how chosing the correct ground structure is critical to obtain a good

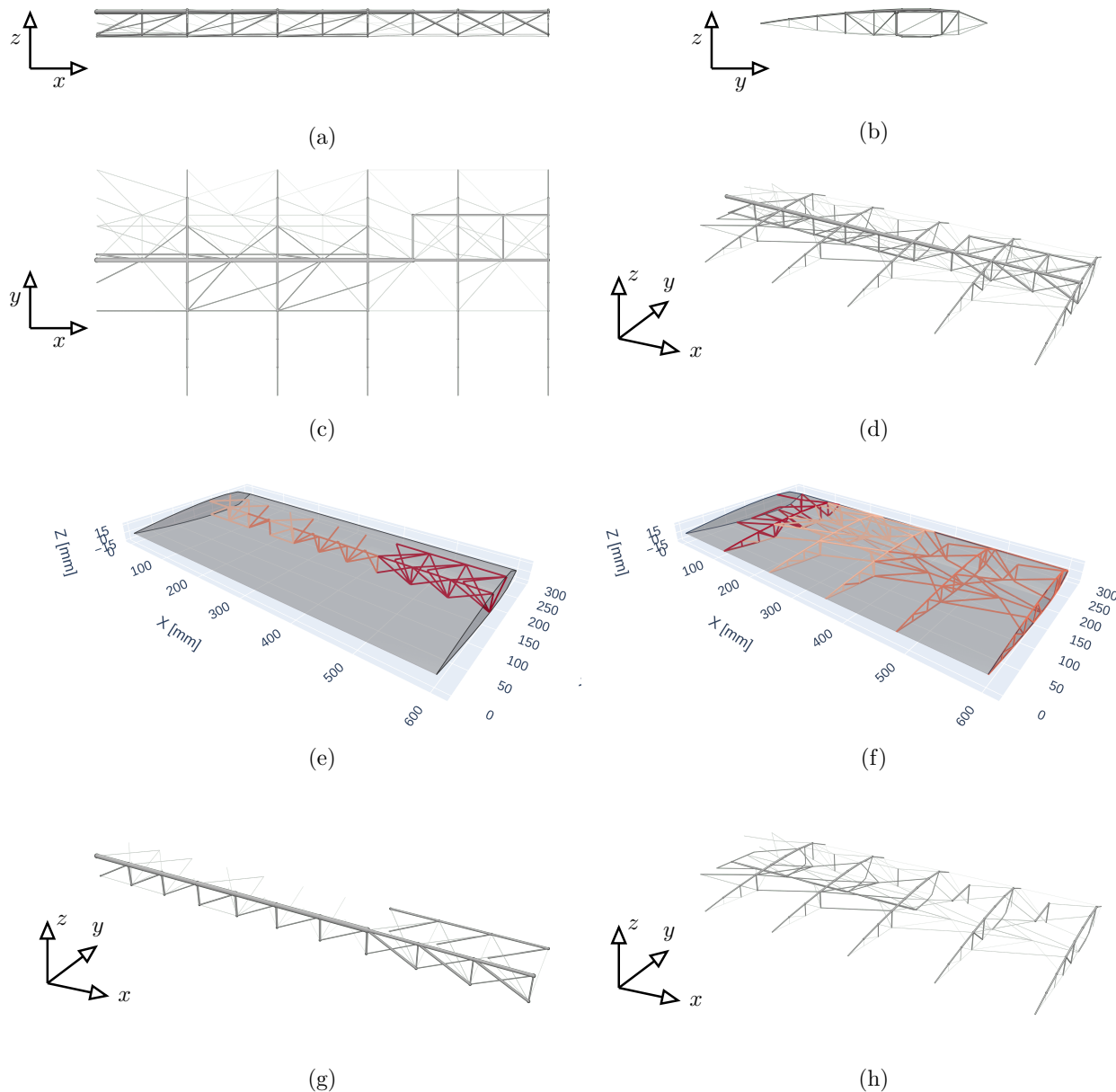


**Figure 1.14**

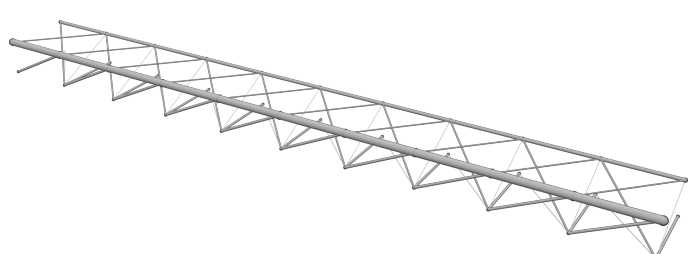


**Figure 1.15**

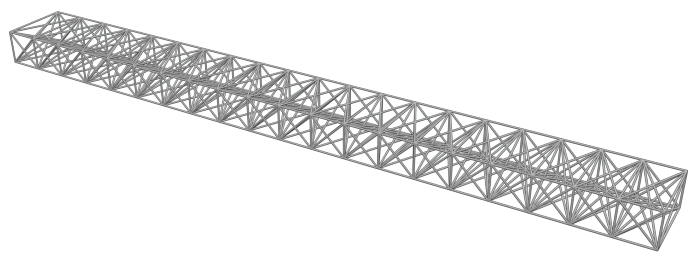


Figure 1.16

solution .

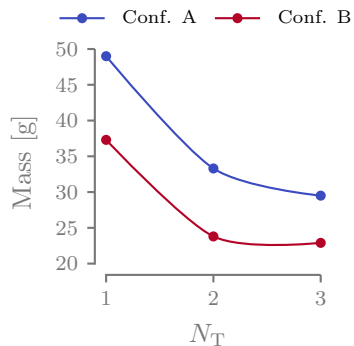


Figure 1.17

Finally, in Fig. 1.18 we present the optimization resulting structure obtained for configuration B and with  $N_T = 3$  different topologies for the wingbox and the section type modules. The structure present a total mass  $M = 22.9$  g and a mass density of  $\bar{\rho} = 5.38$  kg/m<sup>3</sup>. Subfigure (a) shows the isometric view of the optimized topology. The structure shows exactly the same characteristics as the configuration case A, with all similar ribs and a single big spar that is split two towards the end of the span. However, the similarity ends when observing the wingbox type subdomains in subfigures (b) and (d). Here we see how the reduced buckling length given by the higher number of submodules help reducing the cross-sectional area of the big spar. The layout of the modules is shown in subfigures (b) and (c) for the two modules types. Compared to the configuration A results we notice a more even distribution, signs that the optimization runs correctly.

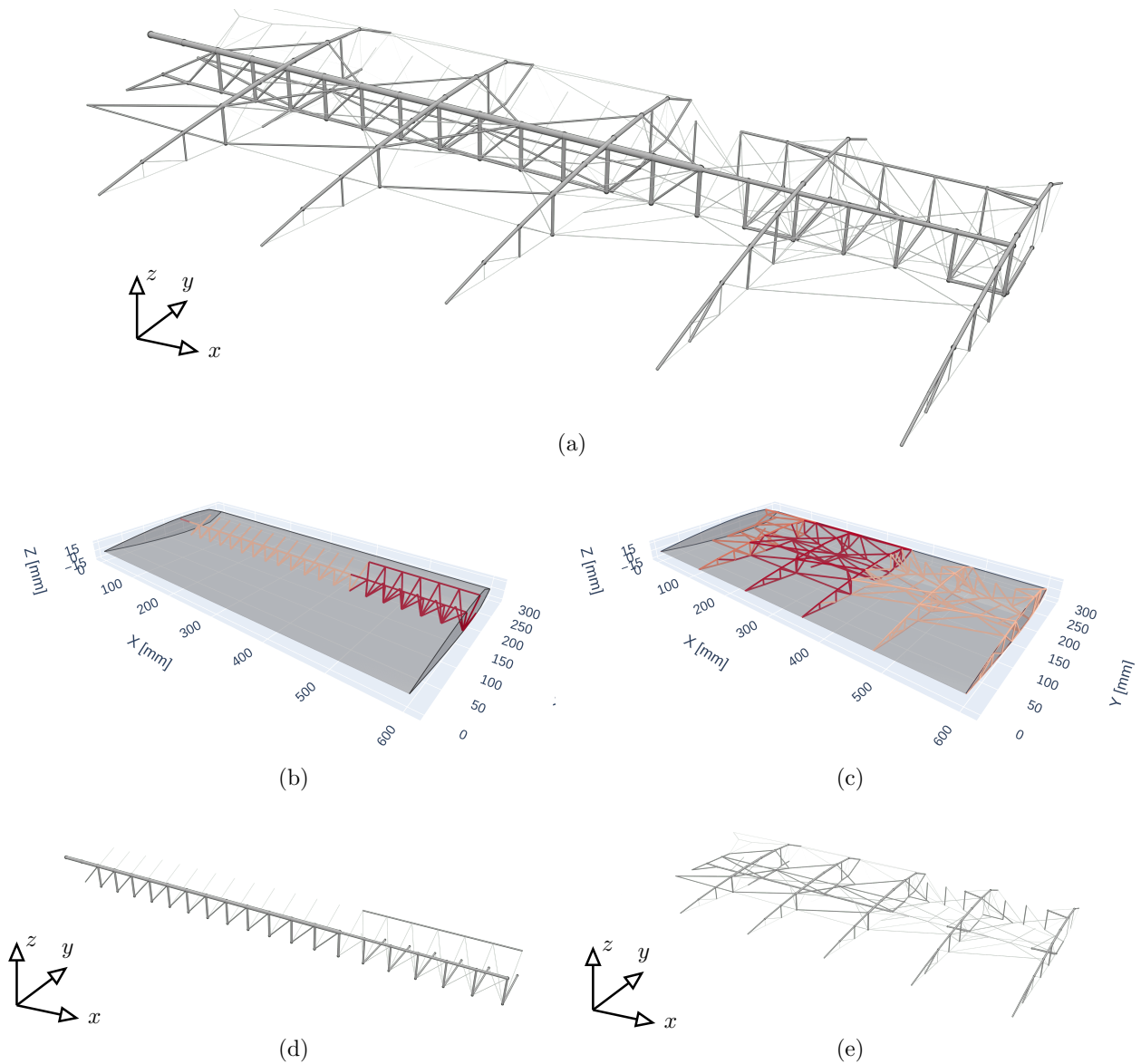


Figure 1.18

### **1.3 CONCLUSION**

## BIBLIOGRAPHY

- [1] Cramer, N. B., Cellucci, D. W., Formoso, O. B., Gregg, C. E., Jenett, B. E., Kim, J. H., Lendraitis, M., Swei, S. S., Trinh, G. T., Trinh, K. V., and Cheung, K. C., 'Elastic shape morphing of ultralight structures by programmable assembly', *Smart Materials and Structures* 28.5 (Apr. 2019), p. 055006.  
DOI: [10.1088/1361-665X/ab0ea2](https://doi.org/10.1088/1361-665X/ab0ea2) cited on pages 1, 16
- [2] Opgenoord, M. M. and Willcox, K. E., 'Aeroelastic Tailoring using Additively Manufactured Lattice Structures', *2018 Multidisciplinary Analysis and Optimization Conference*, Atlanta, Georgia: American Institute of Aeronautics and Astronautics, June 2018.  
DOI: [10.2514/6.2018-4055](https://doi.org/10.2514/6.2018-4055) cited on page 1
- [3] Opgenoord, M. M. J. and Willcox, K. E., 'Design for additive manufacturing: cellular structures in early-stage aerospace design', *Structural and Multidisciplinary Optimization* 60.2 (Aug. 2019), pp. 411–428.  
DOI: [10.1007/s00158-019-02305-8](https://doi.org/10.1007/s00158-019-02305-8) cited on page 1
- [4] Shahabsafa, M., Mohammad-Nezhad, A., Terlaky, T., Zuluaga, L., He, S., Hwang, J. T., and Martins, J. R. R. A., 'A novel approach to discrete truss design problems using mixed integer neighborhood search', *Structural and Multidisciplinary Optimization* 58.6 (Dec. 2018), pp. 2411–2429.  
DOI: [10.1007/s00158-018-2099-8](https://doi.org/10.1007/s00158-018-2099-8) cited on page 1
- [5] Brooks, T. R., Kenway, G. K. W., and Martins, J. R. R. A., 'Benchmark Aerostructural Models for the Study of Transonic Aircraft Wings', *AIAA Journal* 56.7 (July 2018), pp. 2840–2855.  
DOI: [10.2514/1.J056603](https://doi.org/10.2514/1.J056603) cited on page 2
- [6] Fakhimi, R., Shahabsafa, M., Lei, W., He, S., Martins, J. R. R. A., Terlaky, T., and Zuluaga, L. F., 'Discrete multi-load truss sizing optimization: model analysis and computational experiments', *Optimization and Engineering* (Sept. 2021).  
DOI: [10.1007/s11081-021-09672-6](https://doi.org/10.1007/s11081-021-09672-6) cited on pages 2–4
- [7] Stragiotti, E., 'Truss Topology Optimization with Topological Buckling Constraints Data Set', May 2023.  
DOI: [10.17632/BW7XB2W6ST.1](https://doi.org/10.17632/BW7XB2W6ST.1) cited on page 2
- [8] Diamond, S. and Boyd, S., 'CVXPY: A Python-Embedded Modeling Language for Convex Optimization', 2016.  
cited on page 2
- [9] Domahidi, A., Chu, E., and Boyd, S., 'ECOS: An SOCP solver for embedded systems', *2013 European Control Conference (ECC)*, Zurich: IEEE, July 2013, pp. 3071–3076, ISBN: 978-3-033-03962-9.  
DOI: [10.23919/ECC.2013.6669541](https://doi.org/10.23919/ECC.2013.6669541) cited on page 2
- [10] Moore, J. K. and Mechmotum, 'cyipopt: Cython interface for the interior point optimizer IPOPT', 2018.  
cited on page 2

URL: <https://github.com/mechmotum/cyipopt>

cited on page 2

- [11] Wächter, A. and Biegler, L. T., 'On the implementation of an interior-point filter line-search algorithm for large-scale nonlinear programming', *Mathematical Programming* 106.1 (Mar. 2006), pp. 25–57.

doi: [10.1007/s10107-004-0559-y](https://doi.org/10.1007/s10107-004-0559-y)

cited on page 2

- [12] Alappat, C., Basermann, A., Bishop, A. R., Fehske, H., Hager, G., Schenk, O., Thies, J., and Wellein, G., 'A Recursive Algebraic Coloring Technique for Hardware-efficient Symmetric Sparse Matrix-vector Multiplication', *ACM Transactions on Parallel Computing* 7.3 (2020), 19:1–19:37.

doi: [10.1145/3399732](https://doi.org/10.1145/3399732)

cited on pages 7, 16

- [13] Ashby, M. F., 'Materials selection in mechanical design', 2nd ed. Oxford, OX ; Boston, MA: Butterworth-Heinemann, 1999.  
ISBN: [978-0-7506-4357-3](https://doi.org/10.7506-4357-3)

cited on page 12

- [14] Jenett, B., Calisch, S., Cellucci, D., Cramer, N., Gershenfeld, N., Swei, S., and Cheung, K. C., 'Digital Morphing Wing: Active Wing Shaping Concept Using Composite Lattice-Based Cellular Structures', *Soft Robotics* 4.1 (Mar. 2017), pp. 33–48.

doi: [10.1089/soro.2016.0032](https://doi.org/10.1089/soro.2016.0032)